Jet Propulsion Laboratory
California Institute of Technology

TECHNOLOGY DEVELOPMENT FOR EXOPLANET MISSONS

Technology Milestone Report:
Vortex Coronagraph High Contrast Demonstrations

E. Serabyn, G. Ruane, A.J. Riggs, J. Llop-Sayson, D. Mawet

25 June 2025

National Aeronautics and Space Administration
Jet Propulsion Laboratory
California Institute of Technology
Pasadena, California

Approval page

Prepared by:

E-SIGNED by Eugene Serabyn
on 2025-07-10 08:53:14 GMT

Dr. Eugene Serabyn
Principle Investigator
Senior Research Scientist
NASA/Jet Propulsion Laboratory
California Institute of Technology

Approved by:

E-SIGNED by Brendan Crill
on 2025-07-09 13:38:30 GMT

Dr. Brendan Crill
Deputy Program Chief Technologist
Exoplanet Exploration Program
NASA/Jet Propulsion Laboratory
California Institute of Technology

E-SIGNED by Nicholas Siegler
on 2025-07-09 14:57:24 GMT

Dr. Nicholas Siegler
Program Chief Technologist
Exoplanet Exploration Program
NASA/Jet Propulsion Laboratory
California Institute of Technology

E-SIGNED by Lucas Paganini
on 2025-07-09 16:26:45 GMT

Dr. Lucas Paganini
Program Executive
Exoplanet Exploration Program
Science Mission Directorate
NASA Headquarters

Table of Contents

TDEM Milestone Report:
Broadband light rejection with the optical vortex coronagraph

1. Overview

We report here the results of our 17-SAT17-0015 ROSES Technology Development for Exoplanet Missions (TDEM) project entitled "Vortex Coronagraph High Contrast Demonstrations". Our August 2019 white paper of the same name specified the milestone objectives, success criteria, and methodology for computing the milestone metrics. This report describes the specific components tested, the experimental approach, the optical configurations employed in JPL's Decadal Survey Testbed (DST), the final milestone measurements, and our analysis of the results. We have successfully achieved two of our planned milestones: we have experimentally demonstrated an average contrast level of $(2.49 \pm 0.14) \times 10^{-10}$ for the case of a monolithic aperture in monochromatic light, and an average contrast level of $(4.7 \pm 0.15) \times 10^{-9}$ for the case of a segmented aperture in broadband light of 10% bandwidth.

2. Description of the Technology Milestones

TDEM Technology Milestones are intended to document progress in the development of key technologies for potential space-based missions that would detect and characterize exoplanets, such as the earlier Exo-C [1], Habex [2] and LUVOIR [3] mission concepts, and the 6 m class IR/O/UV exoplanet flagship mission proposed by the recent Astro2020 decadal report [4], currently called the Habitable Worlds Observer (HWO) [5]. This work focuses specifically on the validation of one key TDEM technology – the optical vortex phase mask. Our 17-SAT17-0015 TDEM white paper [6] included four specific milestones targeting different performance areas, which are listed here. The first pair of milestones was aimed at validating vortex performance in the case of unobscured, off-axis, monolithic input apertures:

Milestone 1a: Monochromatic Starlight Suppression with Optical Vortex Phase Masks, for a clear monolithic input pupil

Using optical vortex phase masks and a clear monolithic input pupil, demonstrate a calibrated average coronagraph contrast of 3×10^{-10} (i.e., as deep as the DST currently allows) for at least one polarization state, over angular separations of $3\,\lambda/D$ to $10\,\lambda/D$ from a point source image, for monochromatic light anywhere in the wavelength range 300 –1000 nm.

Milestone 1b: Broadband Starlight Suppression with Optical Vortex Phase Masks, for a clear monolithic input pupil

Using optical vortex phase masks and a clear monolithic input pupil, demonstrate a calibrated average coronagraph contrast of 5×10^{-10} (i.e., as deep as the DST currently allows) for at least one polarization state, over angular separations of $3\,\lambda/D$ to $10\,\lambda/D$ from a point source image, for a 10% bandwidth of light anywhere in the wavelength range 300 –1000 nm.

A second pair of milestones was aimed at validating vortex performance for the case of an unobscured, segmented input aperture:

Milestone 2a: Broadband Starlight Suppression with Optical Vortex Phase Masks, for an unobscured, off-axis segmented input pupil

Using optical vortex phase masks and an unobscured off-axis segmented input pupil, demonstrate a calibrated average coronagraph contrast of 1×10^{-8} or better for at least one polarization state, over angular separations of $3\,\lambda/D$ to $10\,\lambda/D$ from a point source image, for any 10% bandwidth of light in the wavelength range 300 –1000 nm.

Milestone 2b: Broadband Starlight Suppression with Optical Vortex Phase Masks, for an unobscured, off-axis segmented input pupil

Using optical vortex phase masks and an unobscured off-axis segmented input pupil, demonstrate a calibrated average coronagraph contrast of 1×10^{-9} or better for at least one polarization state, over angular separations of $3\,\lambda/D$ to $10\,\lambda/D$ from a point source image, for any 10% bandwidth of light in the wavelength range 300 –1000 nm.

For these demonstrations, our optical vortex phase masks are installed in the focal plane immediately downstream of the pupil stop, which is located on the first of the two deformable mirrors (DMs) in our DST setup. The "angular separations" are defined in terms of the wavelength λ and the diameter D of the aperture stop on the deformable mirror (DM), which is the pupil-defining element of the laboratory coronagraph. Our performance metric is the average contrast in the dark hole region specified in the milestones. Contrast is defined (section 5) for any point in the field as the calibrated ratio of the residual light level at that location to the light level at the peak pixel of the point source point spread function in the absence of a coronagraphic mask. During the course of this project, we have successfully achieved milestones 1a and 2a.

2.1. Relevance for a Future Exoplanet Mission

Development of optical vortex coronagraph technology is intended to advance the readiness of mission concepts for the coronagraphic imaging and spectroscopic observation of exoplanetary systems. The optical vortex coronagraph has the advantages of a small inner working angle (IWA), high transmission, a clear, undistorted off-axis field of view, and compatibility with the layout of the Lyot coronagraph [7-9]. The small IWA capability of the vortex coronagraph allows consideration of a range of telescope sizes [10], and vortex coronagraphs have been selected either as primary or secondary coronagraphs by both the recent Habex and LUVOIR mission concept studies [2,3], as well as by the Astro2020 exoplanet flagship mission concept [4]. The vortex coronagraph is thus of particular relevance to the future HWO mission.

In reflected light, terrestrial exoplanets are expected to be only $\approx 10^{-10}$ as bright their host stars, while super-Earths and Jovians can have reflected-light flux ratios of $\approx 10^{-9}$. To detect such exoplanets, image plane contrasts must be comparable, and this TDEM project aimed at image plane contrasts compatible with such super-Earth and Jovian detections, and also with the limit of the DST testbed. In the following, we use "contrast" to mean the raw detected image-plane flux ratio between off-axis positions in a point source's point spread function (PSF) and the on-axis peak signal. It is expected that post-processing of coronagraph data will improve detection sensitivities to planets and debris disks by roughly

an order of magnitude [11], but that aspect is not addressed by this project; i.e., our contrast refers to the raw (unprocessed) contrast in the dark field.

Our contrast specification relates to the average contrast level in a specified dark field of interest around a laboratory source or host star, which should be applicable to any coronagraph that relays a field of view on the sky to the instrumental focal plane without optical distortions. Exoplanet imaging missions form a high contrast "dark hole" or "dark field" over working angles spanning $n_i\lambda/D$ to $n_o\lambda/2D$, where $n_i\lambda/D$ corresponds to the inner working angle (IWA), as defined by the science requirements and the wavefront control algorithm, and $n_o\lambda/D$ corresponds to the outer working angle (OWA) of the targeted dark hole, i.e., the outermost radius to which the wave front control algorithm is applied. The earlier TPF-C science requirements were an IWA of $4\lambda/D$ [12], but as smaller values are possible with the vortex coronagraph, we selected $3\lambda/D$ for our IWA in this work. The OWA was chosen as $10\lambda/D$, to be consistent with other TDEM work. This OWA is not an experimental limitation in any sense, as earlier dark-hole demonstrations and extensive optical modeling and tolerancing have shown that dark-field contrasts for the vortex coronagraph generally improve with distance from the image of the target star. Thus, lowering the average contrast simply by increasing the OWA further is without real benefit.

Analysis of contrast in the dark field must necessarily account for the statistical nature of the static and "quasi-static" speckles present. Experimentally, speckles will show a distribution of intensities, from which the average dark-hole contrast and statistical confidence levels can be estimated. Statistical measures of both the average intensity and its variance in the coronagraphic dark field are specified in Section 4.

2.2. Vortex Coronagraph Theory

The operation of an ideal optical vortex coronagraph is described in, e.g., [13-15]. A clear telescope input pupil can be described by a field distribution, $P_i(r)$, of

$$P_i(r) = \begin{cases} 1 & \text{for} \quad r < a \\ 0 & \text{for} \quad r > a, \end{cases} \tag{1}$$

where r is the radial coordinate, and a is the radius of the input aperture. Focusing the light leads, via a Fourier transform, to the usual focal-plane field distribution,

$$E_f(\theta) \propto \frac{J_1(ka\theta)}{ka\theta}, \tag{2}$$

where J_1 is the Bessel function of order 1, k is the wavenumber, and θ is the angular radial offset from the center of the stellar PSF.

Passing this focal plane field distribution through a centered optical vortex phase mask multiplies the field by a phase factor corresponding to an azimuthal phase ramp, i.e., $n\alpha$, where α is the azimuthal angle, and n is the "topological charge" of the vortex (i.e., the number of 2π's of phase the mask generates for one circuit about the center), yielding

$$E_f(\theta, \alpha) \propto e^{in\alpha} \frac{J_1(ka\theta)}{ka\theta}. \tag{3}$$

After the vortex phase mask, the light is recollimated and forms a downstream pupil image. Because of the Fourier transform relationship between focal and pupil planes, the vortex's phase wrap, and the following property of Bessel functions, J_n, of order n,

$$J_n(x) = \int_{-\pi}^{\pi} e^{-i(n\varphi - x\sin(\varphi))}\, d\varphi, \tag{4}$$

the reimaged pupil plane distribution is proportional to [13-15]

$$\int_0^{\infty} J_n(kr\theta) J_1(ka\theta) d\theta \tag{5}$$

instead of the usual

$$\int_0^{\infty} J_0(kr\theta) J_1(ka\theta) d\theta. \tag{6}$$

This modest change to the integrand alters the downstream pupil intensity distribution dramatically, in the ideal case (and for even n) moving all of the light originally inside the entrance pupil to its outside (Fig. 1, top right panel.) Outside the post-vortex pupil, the electric field falls off as rippled power laws, leading to multiple azimuthal rings for n > 2. In the ideal case, the starlight can then be completely blocked by a simple aperture stop in the downstream pupil plane with a radius slightly smaller than the pupil image radius. However, if wavefront aberrations are present, residual light will appear inside the pupil.

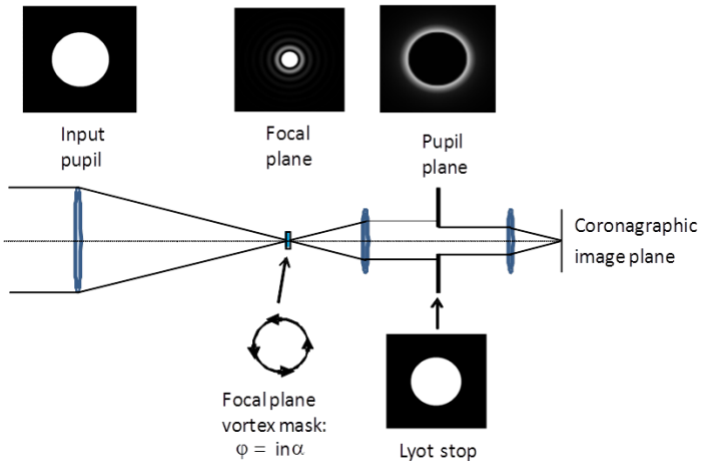

Figure 1. *Layout of the optical vortex coronagraph: an optical vortex phase mask in the focal plane yields a downstream pupil image in which all of the on-axis starlight appears outside of the original pupil's image, where it is blocked by an aperture (Lyot) stop.*

3. The essential components and the testbeds

3.1.1 Vector Vortex Mask Fabrication

An ideal vector-vortex phase mask is a half-wave plate with a spatially-variant fast-axis orientation angle that is given by qα, where α is the azimuthal angle and q is an integer.

This provides the output beam with a geometric phase of $\pm n\alpha$ in the two circular polarization states, where $n = 2q$ is the topological charge of the vortex.

Different techniques of fabricating such vortex phase masks are discussed in [16]. For this project we have developed vector vortex phase masks made of liquid crystal polymer (LCP) layers [9,15], due to their manufacturability and applicability to short (i.e., near-infrared, visible and near-ultraviolet) wavelengths. Our LCP vortex masks were manufactured by Beam Engineering (Beamco). To achieve an achromatic half-wave phase shift across a 10% spectral band, Beamco relies on a well-known multi-layer achromatization technique (Fig. 2), in which three successive HWP layers are rotated relative to each other by ≈ 60° [17, 18]. The mask used here was composed of three such individually-rotated HWP layers, each of which is itself made up of a small number of ~ hundred-nanometer thick sub-layers that are laid down sequentially. Each HWP layer is uniform in the vertical direction (i.e., perpendicular to the vortex plane), but follows the vortex fast-axis orientation pattern laterally. The result is a relatively achromatic HWP that is approximately 1 μm thick. The LCP layers are encapsulated between two glass substrates with anti-reflective coatings applied on the external surfaces, as is illustrated in Fig. 3.

Fig. 4 shows the sequence of fabrication steps involved in making a multi-layer vortex mask [19]. As this figure suggests, the production of such masks requires great care to achieve high levels of layer accuracy and quality.

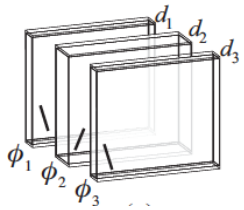

Figure 2. *Classical uniform multilayer approach to broadening waveplate passbands [17]. The three individual optical axis orientations are shown.*

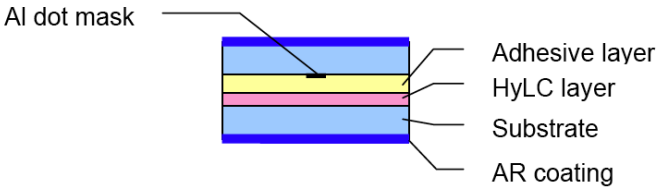

Figure 3. *Cross-section of the sandwich design of our usual liquid crystal polymer vortex masks. The hybrid liquid crystal polymer (HyLC) layer is situated between two glass disks.*

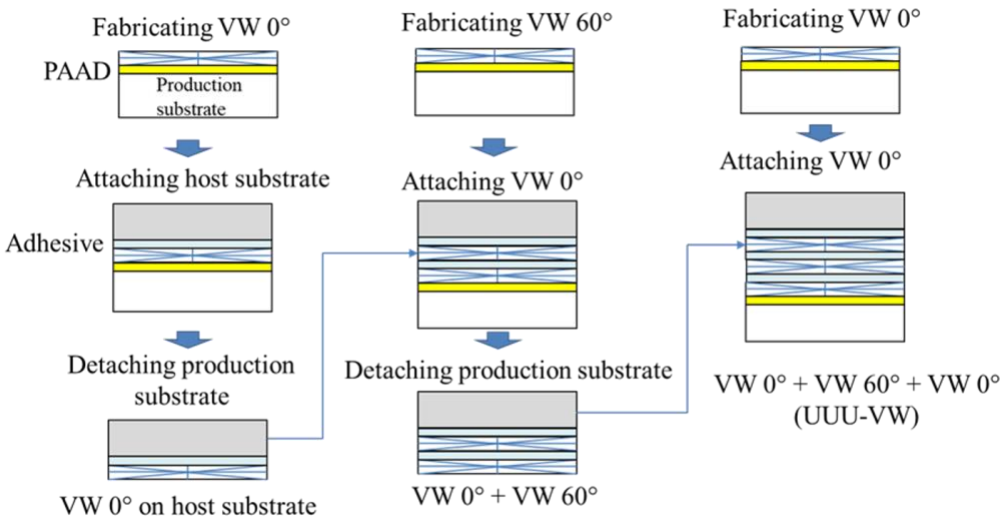

Figure 4. *Fabrication steps of a three-layer broadband vortex mask [19]. VW stands for vortex waveplate.*

3.1.2 Vortex Mask Characterization

While several vortex masks were obtained and tested over the course of this work, the best contrast results were achieved in the DST with the mask with part no. V650-BW10-Q2-UUU-CDD15-OD7(2)), as in our earlier work. The mask is a charge 4 vortex mask, designed to be achromatic over a bandwidth of at least $\Delta\lambda/\lambda = 10\%$ centered at 650 nm. The central phase singularity in most of our masks is blocked by a small metallic circular occulter, but this particular mask did not include an opaque blocker. The complete set of mask specifications, as ordered, are listed in Table 1. Refs. [20] and [21] describe this mask and its performance in more detail.

We first characterized the vortex mask using a Mueller matrix spectro-polarimeter (MMSP; Axometrics Axostep) that measures the full Mueller matrix (MM) for transmitted light at each pixel in a microscope image of the mask roughly 3 mm across at several visible wavelengths, using diffuse transmitted illumination. In our setup, the MM measurements were at wavelengths of 450-800 nm in sequential steps of 50 nm at a spatial sampling of 5.8 μm per pixel for 128 x160 pixels (or 0.74 x 0.93 mm).

Figure 5a shows the measured geometric phase shift for one circular polarization, as calculated from the measured orientation of the fast axis at $\lambda = 650$ nm. We fit the expected geometric pattern to the measured pattern to numerically determine the vortex center and azimuthal rotation angle offset (Fig. 5b). As the MMSP cannot distinguish between fast axis orientations differing by π radians, we unwrapped the fast axis angles by adopting the π-offset that gives a phase shift that best matches the vortex pattern at each pixel. We then subtracted the best fit vortex phase pattern to determine the errors in the phase pattern due to fast axis orientation errors (Fig. 5c). We find that the phase error is centrally peaked and slightly asymmetric with a peak of $\sim \pi/10$. The first $\pi/40$ contour occurs at approximately

122 μm from the center and π/20 is exceeded within the inner southwest lobe at a maximum radius of 52.3 μm.

Table 1: Vortex Mask Specifications

Quantity:	
Substrate:	
material	Glass index matched to average index of the LCP material Glass must have no birefringence
diameter	1 inch round substrates; diameter not to exceed 1 inch after gluing
thickness	~ 2 – 3 mm; thinner is better, but not required
surface quality	λ/10 requirement; λ/20 rms desirable
Optical properties:	
Center wavelengths	650 nm
Bandwidth	At least 10%, i.e., 617.5 – 682.5 nm
Retardance requirement	180° +/- 1° over the desired 10 % band
Retardance goal	180° +/- 0.1° over the desired 10 % band
Angle of incidence	Normal incidence
AR coating	R < 0.1 % across the 10% band of interest (with 0.01% goal)
Total transmission	≥ 90% within the 10% band of interest
Clear aperture	80-90%
Device structure:	
Vertical structure	AR/substrate/black-dot/adhesive/LCP-layers/substrate/AR
LCP layer structure	3 devices with uniform rotated layers (UUU); 1 device at each of the three central wavelengths specified: 550 nm, 650 nm, and 750 nm
Device q	q = 2 (i.e., LCP fast axis orientation = 2x azimuthal angle)
Central vortex defect diameter	< 5 microns; the smaller the better
Front/back discrimination	Substrates with black dot and vortex layers are to be identified with marks on the sides of their respective substrates
Central opaque dot:	
Central opaque dot diameter	15 microns
Centration of opaque dot	Opaque dot centered over central defect to ~ 1 micron
Central opaque dot quality	No splattering of dot material beyond geometric dot
Central opaque dot transmission	$< 10^{-7}$ if possible

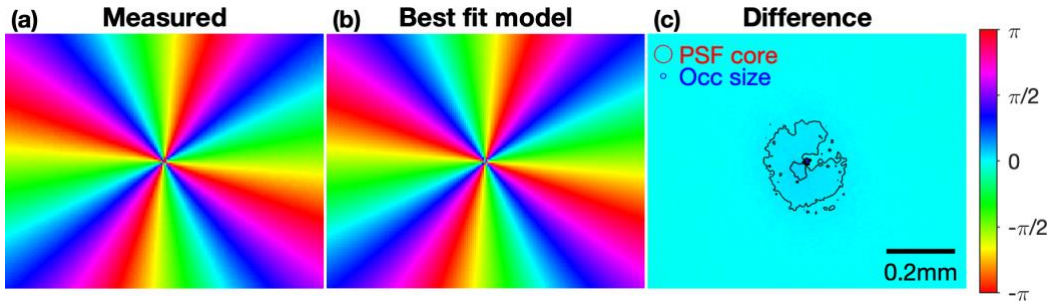

Figure 5. *Vortex mask phase pattern characterization at λ = 650 nm. (a) Geometric phase shift derived from the measured fast axis orientation. (b) The best fit model of the vortex phase pattern. (c) The difference between (a) and (b). The red circle shows the size of the point spread function (PSF) core in the testbed configuration presented below (i.e., an angular radius of 1.22 λ/D corresponding to the first null in the Airy pattern). The contour lines show phase steps of π/40.*

We also used the MMSP to measure the retardance near the center of the device. Figures 6a-d show the resultant retardance maps at wavelengths of 550, 600, 650, and 700 nm. While an ideal vortex mask would have 180° retardance everywhere for all wavelengths, this mask shows a relatively uniform retardance that is wavelength dependent, with a median retardance error < 2° within a $\Delta\lambda/\lambda = 0.1$ passband centered near 635 nm (Fig. 6e). Table 2 provides the retardance error statistics determined from these MMSP images. In the following, we use $\lambda_0 = 635$ nm as the central wavelength, which is slightly smaller than the design wavelength of $\lambda_d = 650$ nm, to make use of the band with the lowest bulk retardance error. In addition, a cross-like defect is seen near the center of the mask at all wavelengths (indicated by fiducial hash marks), as well as small variations at high spatial frequencies. The former is likely produced by limitations of the MMSP, as it has been found to decrease in size with increasing magnification and rotational sampling.

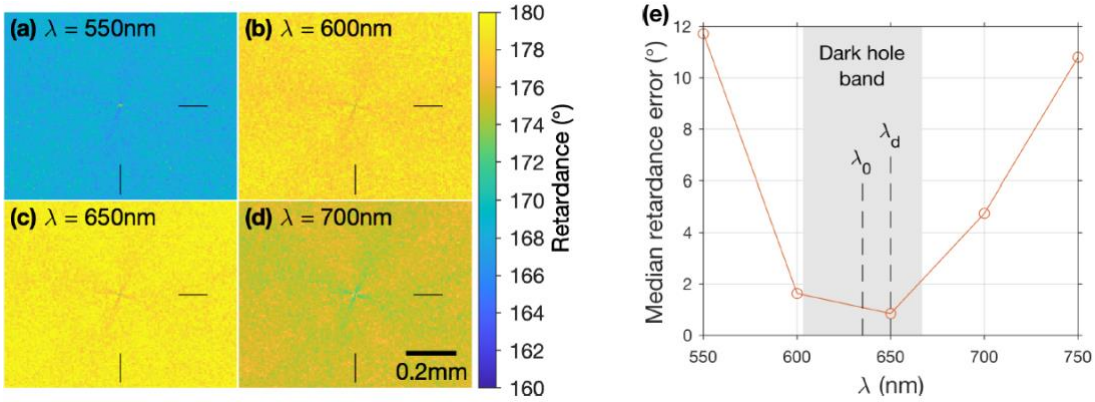

Figure 6. *Focal plane mask retardation measurements. (a)-(d) Retardance maps at wavelengths of (a) 550, (b) 600, (c) 650, and (d) 700 nm. (e) Median retardance error within images shown. The grey area shows the wavelength range used for the testbed results below, with a central wavelength of 635 nm and a bandwidth of 10%. The design central wavelength of the mask was 650 nm.*

Table 2: Retardance error statistics in Fig. 5.

Wavelength (nm)	Mean retardance (°)	Mean error (°)	RMS error (°)	Std. dev. (°)
550	168.3	-11.7	11.7	0.8
600	178.4	-1.6	1.8	0.8
650	179.1	-0.9	1.1	0.6
700	175.2	-4.8	4.8	0.7

3.1.3 The Segmented aperture mask

The larger the telescope aperture, the more likely it is that its primary mirror will need to be segmented. The HWO space telescope [5] thus may well be segmented, making it important to understand the effect of a segmented pupil on the performance of a vortex coronagraph. Half of our milestones were thus aimed at initial tests of the performance of a vortex coronagraph behind a segmented pupil.

For simplicity in these initial trials, rather than inserting an actual segmented mirror into our beam train, we instead inserted a wire-mesh mask that served to introduce narrow gaps into the beam's initially uniform pupil. By using such a mesh, the resulting pupil segments do not acquire separate piston and tip-tilt errors as they would with a true segmented mirror, but the desired effect, i.e., diffraction from the segment gaps, will be present.

The pupil mask that we used is shown in Fig. 7. It is a freestanding Metglas 2826MB3 metal foil mask etched by United Western Enterprises (UWE), Inc. It has seven segments across the diameter, in a hexagonal pattern. In our experiments, it was stopped down to five segments across the diameter with an iris diaphragm in order to underfill the active surface area of the DM used.

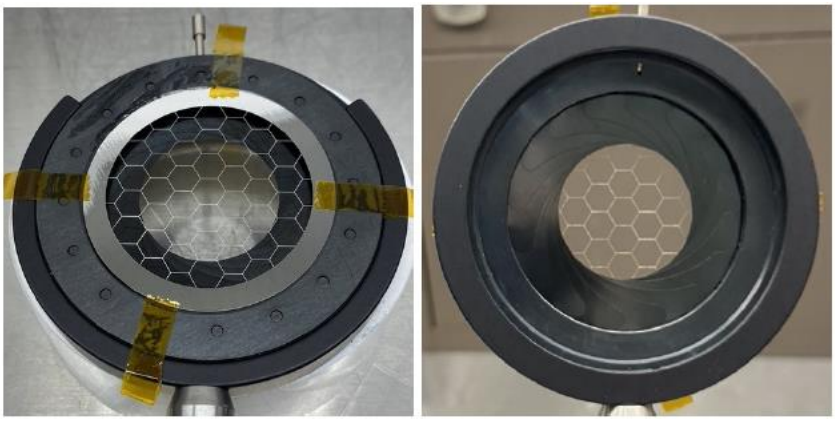

Figure 7: *Back and front views of the mounted segmented pupil mask used in the segmented pupil experiments. A freestanding Metglas metal mask was used to approximate the hexagonal segmentation of a large primary mirror. An iris stopped down the segmented aperture to five segments across in order to slightly underfill the deformable mirror's active surface area.*

3.1.4 Spectral Polarization Filtering

To fully understand the testbed configuration, here we describe the use of "spectral polarization filtering" to broaden the starlight-rejection passband [18]. As described earlier, a vector vortex mask is a spatially variant HWP in which the optical axis orientation is a function of position. A vector vortex is thus achromatic to first order by virtue of the geometry of its structure. A perfect HWP flips circular polarization (CP) states, and the vortex mask's fast-axis orientation pattern provides the desired azimuthal phase pattern in the output CP state that sends that light to the exterior of the downstream pupil, where it is rejected by the Lyot stop. However, the real retardance (Fig. 6) is not exactly 180°, which allows a small fraction of the light to leak through the HWP in the original CP state, unaffected by the vortex phase. In the subsequent pupil plane, this light reimages the original filled pupil, which leads to a faint Airy pattern in the final image plane. This light leak can thus be decreased by filtering out (removing) the initial CP state after the Lyot stop. To carry out this "spectral polarization filtering," it is thus necessary to first select (transmit) one of the two CP states upstream of the vortex, and then to reject that CP state at the end (Fig. 8). To enable spectral polarization filtering, the DST testbed included circular polarizers (comprised of a linear polarizer and quarter wave plate) in the input and output beams (i.e., before and after the vortex mask), the first to enable the selection of a single input CP state, and the second to reject that state at the output.

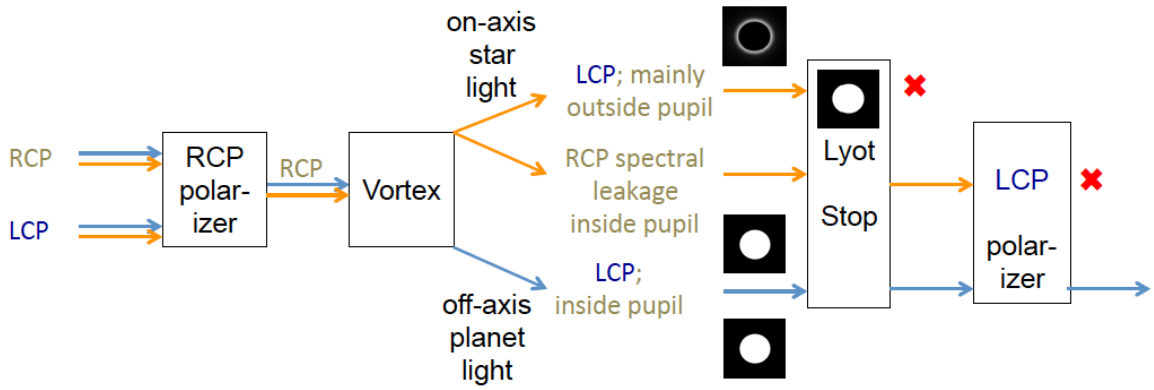

Figure 8. *Spectral polarization filtering. The starlight is shown in orange, and the planet light in blue. RCP and LCP stand for right (left) circular polarization, respectively. The starlight outside the pupil is rejected by the Lyot (aperture) stop, while the spectral starlight leakage inside the pupil is rejected by a circular polarizer.*

3.1.5 The Decadal Survey Testbed

The DST is a coronagraph instrument designed to achieve extremely high contrast (on the order of 10^{-10}) [22]. Details can be found in Patterson et al. 2019 [23]. To achieve maximum stability, the DST is operated in vacuum; a working pressure of ~0.1 mTorr is achieved and maintained for weeks. Temperature variations are on the order of ~10 mK in a cadence of 24h.

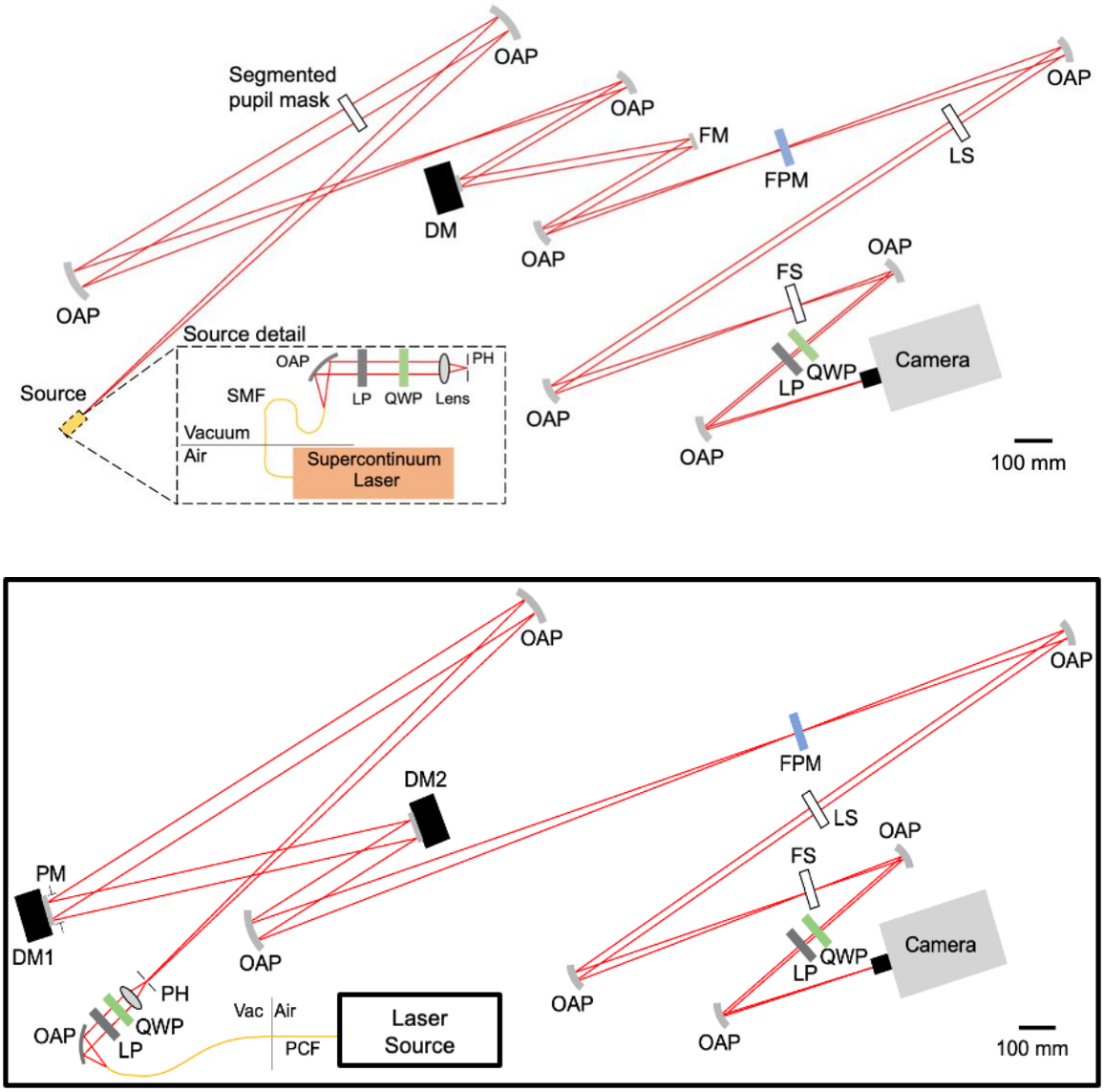

Figure 9. a) *(top) Schematic of the Decadal Survey Testbed (DST) used for the segmented aperture tests. PCF: Photonic Crystal Fiber. SMF: Single mode fiber. Vac: Vacuum. OAP: Off-axis parabolic mirror. LP: Linear Polarizer. QWP: Quarter-wave plate. PH: Pinhole. PM: Pupil mask. DM: Deformable Mirror. FPM: Focal plane mask. LS: Lyot stop. FS: Field stop.* ***b)*** *(bottom) Schematic of the Decadal Survey Testbed (DST). PCF: Photonic Crystal Fiber. Vac: Vacuum. OAP: Off-axis parabolic mirror. LP: Linear Polarizer. QWP: Quarter-wave plate. PH: Pinhole. PM: Pupil mask. DM: Deformable Mirror. FPM: Focal plane mask. LS: Lyot stop. FS: Field stop.*

Due to the evolution of the testbed over the course of this project, the availability of various deformable mirrors, and the need for extra optics in the segmented pupil case, two different testbed configurations were used for milestones 1a and 2a, respectively, as shown in Figures 9a and 9b. Fig. 9a shows the DST layout used for the segmented pupil test, which was carried out first. This configuration provided an extra optical relay in which our pupil mask was inserted. Figure 9b shows the DST layout used for the subsequent monolithic aperture tests, wherein two DMs were used.

Light Source: To simulate the star, a laser (a Thorlabs LP637-SF70 diode laser for the monochromatic demonstrations) or supercontinuum laser source (a NKT SuperK Extreme for the broadband demonstrations) is coupled to a photonic crystal fiber (PCF) that passes through the air-to-vacuum interface. For the supercontinuum source, a remote-control variable filter (NKT Varia) is used to select the source passband (of ∼1% bandwidth). To generate a single CP state, the light exiting the fiber is collimated by an off-axis parabolic mirror (OAP) and passed through a circular polarizer (i.e., a linear polarizer (LP) followed by a quarter wave plate (QWP) with a 45° relative clocking angle). The linear polarizers are Thorlabs LPVIS-100, and the quarter-wave plates are from Tower Optical (SKU: A-25.4-B-.250-C-4; achromatic mounted 25.4 mm). This light is then focused onto a 4 μm diameter pinhole (PH) with an achromatic doublet lens to create a pseudo point source representing a star.

The DMs: The DST was originally commissioned in 2019 with two Xinetics DMs [14]. In 2021, two Boston Micromachines (BMC) 2-k DMs were temporarily installed. The second of those DMs had about a dozen defective actuators that limited performance to no better than 10^{-8} contrast, so it was removed and replaced with a flat mirror in June 2021. The single BMC DM layout shown in Figure 8a was therefore used during the summer of 2021 for the segmented aperture experiments reported herein. For the later monolithic-aperture tests, two DMs manufactured by Northrop Grumman's AOA Xinetics (AOX) were used. They had 48 x48 actuators based on Lead Magnesium Niobate (PMN) electroceramic arrays with 1 mm pitch.

For the monolithic aperture case, the light from the PH was collimated by a 1.52 m focal length OAP towards the first deformable mirror (DM1), where a circular pupil mask (PM; 46.6 mm diameter) defined the entrance pupil. The resolution at a wavelength of 633 nm was 20.5 μm, making this 4 μm pinhole unresolved (its diameter being 20% of the angular resolution). The second deformable mirror (DM2) is located 1 m downstream of DM1.

The coronagraph: After DM2, a second 1.52 m focal length OAP focuses the light onto the focal plane mask (FPM) with a focal ratio of 32.7. The beam transmits through the FPM and a 761 mm focal length OAP creates an image of the pupil with a diameter of 23.3 mm at the position of the Lyot stop (LS). The LS is a circular aperture with a diameter of 18.6 mm (which thus transmits 80% of the geometric pupil diameter). After passing through the Lyot stop, beam is focused onto a small focal-plane field stop (FS), which blocks most of the bright starlight surrounding the desired dark-hole region from reaching the camera plane directly, or from scattering back into the dark hole downstream of the FS plane.

The FS is D-shaped, and offset from the star image, so as to allow a "1-sided" dark hole to be generated next to the star. This is done because a single DM cannot correct both amplitude and phase on both sides of the star, and when this project's guiding white paper was written, only a single DM was foreseen. Moreover, even with two DMs, the contrast

in the DST was found to be a bit better for a 1-sided dark hole. The physical FS actually employed is slightly oversized compared to the desired dark hole extent, with an aperture large enough to accommodate the range of dark hole sizes needed by multiple TDEM projects. Its open aperture is thus a few λ/D larger than our specified dark hole region, the actual size of which (the "scoring region") is selected in software.

After the FS, the light is recollimated by an OAP and passed through a circular analyzer (QWP+LP) to select a single circular polarization state. The light is then focused by a final OAP onto the sCMOS camera (Oxford Instruments Andor Neo 5.5)

Wavefront Correction: The wavefront sensing and correction algorithm that is used to dig a deep dark hole is electric field conjugation [EFC], which is described in detail in [24]. EFC is run with the Fast Linear Least-Squares Coronagraph Optimization (FALCO) [25] software package. For a given waveband, starting with a nominally flat surface figure setting on the DM for each run, we: (a) take a set of contrast field images with the initial DM setting; (b) take images for each of four "probe" DM settings (consisting of small deterministic surface figure deviations from the initial DM setting), (c) use these data to compute the complex electric field in the target 3 – 10 λ/D dark field region, and then (d) calculate and apply a new DM setting to reduce the energy in the dark field. This step also establishes a new "initial DM setting" in preparation for the next iteration of steps a – d.

3.2. Differences Between Flight and Laboratory Demonstrations

There are several important differences between the laboratory demonstration and flight implementation.

Starlight: In a space coronagraph, the spectrum of incident starlight would resemble black body radiation, while here the source was a filtered supercontinuum laser. The laser provides a photon flux that is comparable to or larger than the target stars to be observed. The goal of this milestone was to demonstrate the contrast that can be achieved, without consideration of the source intensity. A bright source is a convenience that does not compromise the integrity of the demonstration, as it affects only integration times.

Unlike the light collected by a telescope from a target star, the intensity of the testbed beam is not completely uniform across the pupil. Typically, this non-uniformity is a center-to-edge drop of a few percent, corresponding to the diffraction pattern from the small pinhole. This small level of non-uniformity is expected to have negligible effect on the final contrast, as the wavefront control algorithm accommodates these small effects without the need for improved illumination uniformity.

Spacecraft dynamics: A control system is required in flight to stabilize the light path against motions of the spacecraft. The dominant effects of spacecraft dynamics are jitter of the star image on the coronagraph focal plane mask and beam walk in the optics upstream of the focal plane mask. As a specific example, the ACCESS analysis [26] showed that for fourth-order coronagraphs (including Lyot and vortex coronagraphs) with an inner working angle of $3\lambda/D$, pointing errors need to be less than ± 0.03 λ/D rms to limit the corresponding contrast degradation to less than 2×10^{-10}. The concept models have shown that the required pointing stability can be achieved in space with current high Technology Readiness Level (TRL) systems. Scaled to the HCIT, this would correspond

to an ability to center the vortex mask on the "star" within 1.5 μm, or about 0.2 pixels when projected to the CCD focal plane. The stability of the testbed, including the centration of the star on the vortex, is untraceable to spacecraft dynamics. In practice, the DST often exhibits alignment drifts that are larger than expected in the space environment, but these tend to decrease with time under vacuum. As such we relied on favorable periods of thermal and mechanical stability of the HCIT.

Polarization separation: In the DST, a single input polarization state is selected by the upstream circular polarizer prior to injection into the testbed through the pinhole. This allows wavefront quality to be unaffected by having the circular polarizer in the beam. On the other hand, in flight, the polarizations may need to be split by a free space optic that could affect wavefront quality. The exact flight configuration is not known, but one way to potentially avoid a free-standing quarter wave plate is to combine a planar QWP device with the vortex mask in a single planar focal plane device. Moreover, other types of vortex phase mask, such as the scalar vortex phase mask, may not require polarization splitting. As such, here we begin with a single-polarization dark hole.

4. Computation of the Metric

4.1. Definitions

The "contrast" metric requires measurement of the intensity of the dark-hole speckle field relative to the intensity of the central star. The contrast can be assessed in terms of statistical confidence to capture the impact of experimental noise and uncertainties. Here we define the terms involved and describe the measurements and data products.

4.1.1. "Raw" Image and "Calibrated" Image. Standard techniques for the acquisition of CCD images are used. A "raw" image is defined as the pixel-by-pixel image obtained by reading the charge from each pixel of the CCD, and amplifying and sending it to an analog-to-digital converter. A "calibrated" image is defined as a raw image that has had background bias subtracted. Saturated images are avoided in order to avoid the confusion of CCD blooming and other potential CCD nonlinearities. All raw images are permanently archived and available for later analysis.

4.1.2. "Scratch" is a DM setting in which actuators are set to a predetermined surface figure that is approximately flat (~ 20 volts on each actuator).

4.1.3. Our "star" is a small (4-μm diameter) pinhole illuminated with light relayed via optical fiber from a source outside the HCIT vacuum wall. The pinhole is roughly 20% of Fλ at 633 nm. This "star," the only source of light in the optical path of the HCIT, is a stand-in for the star image that would have been formed by a telescope system.

4.1.4. The "algorithm" is the computer code that takes as input the measured speckle field images, and produces as output a voltage value to be applied to each element of the DM, with the goal of reducing the intensity of speckles.

4.1.5. The "contrast field" is a dimensionless map representing, *for each pixel of the detector*, the ratio, r, of its measured intensity to the value of the peak of the central stellar PSF that is measured in the same testbed conditions (light source, exposure time, Lyot stop, etc.) when the focal plane vortex mask is removed.

4.1.6. The "average contrast," c_i, for the i[th] dark hole in a sequence of dark holes, is a dimensionless quantity that is the average value of the contrast field over the pixels in the dark hole specified i.e.,

$$c_i = \frac{1}{m}\sum_{1}^{m} r_m,$$

where m is the number of pixels in the selected dark hole.

4.1.7. "Statistical Confidence". The interpretation of measured numerical contrast values shall take into consideration, in an appropriate way, the statistics of measurement, including detector read noise, photon counting noise, and dark noise.

The milestone objective is to demonstrate with 90% statistical confidence that the true contrast value in the dark field, as estimated from our measurements, is equal to or better than the required threshold contrast value C_0. The estimated true contrast value shall be obtained from the average of the set of four or more contrast values measured in a continuous sequence (over an expected period of approximately one hour). Estimation of the statistical confidence level requires an estimation of variances. Given that our speckle fields contain a mix of static and quasi-static speckles (the residual speckle field remaining after the completion of a wavefront sensing and control cycle, together with the effects of alignment drift following the control cycle), as well as other sources of measurement noise including photon statistics and CCD read noise, an analytical development of speckle statistics is impractical. Our approach is to compute the confidence coefficients on the assumption of Gaussian statistics.

At any time in the demonstration, the instantaneous contrast is subject to laboratory conditions, including the quality of the optical components, their alignment, any drift in their alignment over time, and the effectiveness of each wavefront sensing and control cycle. With each iteration, our nulling procedure attempts to improve the contrast value, thus compensating for any drift or changes in alignment that may have occurred since the previous iteration, and further variations may be expected due to experimental noise and any limitations in the algorithm. The data set built up from a sequence of such iterations provides a distribution of contrast values, which will be regarded as Gaussian about a mean contrast for the data set. We therefore consider the mean contrast value as representative of the true contrast value for a data set, and the distribution of contrast determinations among the iterations within the data set as a combination of both random wavefront control errors and random measurement errors. The mean contrast values and confidence limits are computed as follows. The average contrasts, c_i, of each of the last few (n) images in an iteration sequence are averaged to compute what we call the *mean contrast value*, $\hat{c}$, via

$$\hat{c} = \frac{1}{n}\sum_{i=1}^{n} c_i.$$

(Note that $\hat{c}$ is thus the temporal average of the spatially-averaged dark-hole contrasts.)

The standard deviation σ_{each} in the contrast values c_i obtained for individual images within the set, which includes both the measurement noise and the (assumed random) contrast variations due to changes in the DM settings for each speckle nulling iteration, is:

$$\sigma_{each} = \sqrt{\sum_{i=1}^{n} \frac{(c_i - \hat{c})^2}{n-1}}$$

The measurement uncertainty of the mean contrast estimate $\hat{c}$ is thus $\sigma_{mean} = \sigma_{each} / \sqrt{n}$. To this uncertainty must be added the systematic uncertainty in quadrature, making the net standard deviation

$$\sigma = \sqrt{\sigma_{mean}^2 + \sigma_{sys}^2}$$

Note that the systematic error may itself be comprised of several terms added in quadrature.

4.1.8. "Statistical Confidence". For contrast values that have a Gaussian distribution about the mean contrast, the statistical confidence that the mean contrast ĉ is less than some value c_0 is given by

$$conf(z < t) = \frac{1}{\sqrt{2\pi}} \int_{-\infty}^{t} e^{-z^2/2}\, dz = \frac{1}{2} + \frac{1}{\sqrt{2\pi}} \int_{0}^{t} e^{-z^2/2}\, dz$$

where $t = (c_0 - \hat{c})/\sigma$. Thus, as $\hat{c} = c_0 - t\sigma$, meeting a milestone contrast target c_0 with the desired confidence level requires the final measured mean contrast for a given run, ĉ, to be lower than the target contrast c_0 by t standard deviations. The Gaussian integral is widely tabulated, and *conf* = 0.9 implies t = 1.28, or $\hat{c} = c_0 - 1.28\sigma$. I.e., the measured ĉ must be smaller than the target c_0 by at least 1.28σ.

4.2. Measurement of the Star Brightness

The raw contrast is approximated by the "normalized intensity" defined by the stellar intensity normalized to the peak of the full on-axis point spread function, which was measured prior to each wavefront control trial by offsetting the focal plane mask by 1mm (leaving all other optical elements in place) and taking an unsaturated short-exposure image. A typical flux level was ~1e8 photons per second per pixel at the PSF peak, though this changes with wavelength and time due to slow drifts in the system.

4.3. Measurement of the Coronagraph Contrast Field

Each "coronagraph contrast field" is obtained as follows:

4.3.1. The vortex mask is centered on the star image.

4.3.2. An image (typical exposure times for the milestone runs were 2 min) is taken of the coronagraph field (the suppressed star and surrounding speckle field). The dimensions of the target areas, as shown schematically in Fig. 10, are a dark (D-shaped) field extending from 3 to 10 λ/D, which is bounded by a straight line that passes 3 λ/D from the star at its closest point, and by a circle of radius 10 λ/D centered on the star.

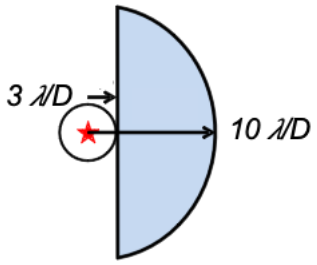

Figure 10. *Target high-contrast dark field from 3 to 8 λ/D, as described in the text. The location of the suppressed central star is indicated in red.*

4.3.3. Each coronagraph image is normalized to the peak "star brightness", as defined earlier, by the fixed relationship between peak star brightness and the integrated light in the speckle field outside the central DM-controlled area.

4.3.4. The mean contrast is the sum of all pixel contrast values in the dark field area, divided by the total number of pixels in the dark field area, with no weighting applied, as discussed in Section 4.1.7. The rms of the contrast in the dark-hole field is based on these same pixel values.

4.4. Milestone Demonstration Procedure

The procedure for the milestone demonstration is as follows:

4.4.1. The DM is set to scratch. An initial coronagraph contrast field image is obtained as described in Sec. 4.1.

4.4.2. Wavefront sensing and control is performed to find settings of the DM actuators that give the required high-contrast in the target dark field. This iterative procedure may take from one to several hours, starting from scratch, if no prior information is available. It can also take more or less time depending on the stability of the HCIT optical system.

4.4.3. A number of contrast field images are then taken, yielding a sequential set of contrast field images. It is required that a sufficient number of images are taken to provide statistical confidence that the milestone contrast levels have been achieved, as described in Section 4.1.7.

4.4.4. Laboratory data are archived for future reference, including raw and calibrated images of the reference star and contrast field images.

5. Success Criteria

The following are the required elements of the milestone demonstration. Each element includes a brief rationale.

5.1. Illumination is either near-monochromatic or 10% percent light in single or dual polarization at a wavelength in the range of 400 nm $< \lambda <$ 900 nm, depending on the particular milestone.

Rationale: *This milestone is an initial demonstration of the feasibility of the approach at a wavelength in the science band of TPF-C or Exo-C.*

5.2. The mean contrast specified in the milestone list or smaller shall be achieved in a 3 to 10 λ/D dark zone, as defined in Sec. 3.3.2.

Rationale: *This provides evidence that the high contrast field is sufficiently dark to be useful for searching planets, and to carry out initial tests at small angles.*

5.3. The milestone contrast level, averaged over the data set, shall be met with a confidence of 90% or better, as defined earlier. Sufficient data must be taken to justify this statistical confidence.

Rationale: *Assuming the contrast values have a Gaussian distribution about the mean contrast, this demonstrates a statistical confidence of 90% that the mean contrast goal has been reached.*

5.4. Elements 4.1 – 4.3 must be satisfied on three separate occasions with a reset of the wavefront control system software (DM set to scratch) between each demonstration.

Rationale: *This provides evidence of the repeatability of the contrast demonstration. The wavefront control system software reset between data sets ensures that the three data sets can be considered as independent and do not represent an unusually good configuration that cannot be reproduced. For each demonstration the DM will begin from a "scratch" setting. There is no time requirement for the demonstrations, other than the time required to meet the statistics stipulated in the success criteria. There is no required interval between demonstrations; subsequent demonstrations can begin as soon as prior demonstrations have ended. There is also no requirement to turn off power, open the vacuum tank, or delete data relevant for the calibration of the DM influence function.*

6. Certification

The PI will assemble a milestone certification data package for review by the ExEP TAC and the ExEP program. In the event of a consensus determination that the success criteria have been met, the project will submit the findings of the review board, together with the certification data package, to NASA HQ for official certification of milestone compliance. In the event of a disagreement between the ExEP project and the ExEP TAC, NASA HQ will determine whether to accept the data package and certify compliance or request additional work.

7. Demonstration Results

7.1. Milestone 2a Certification Data Package: Broadband Starlight Suppression for an unobscured, off-axis segmented input pupil

This section presents our contrast results with a segmented off-axis aperture, 10% bandwidth light, the 1-DM layout of Fig. 9a, and the entrance pupil mask of Fig. 7. This work is described in ref. [27].

First, pupil intensity images were obtained using a retractable pupil imaging lens just before the detector, for both the original clear pupil and the segmented pupil, as shown in Fig. 11. The pupil diameter for the segmented case was ≈ 4% larger in order to fit exactly five segments across. This had the effect of making visible some DM surface "scalloping" near the edge of the pupil. Scalloping is the uncorrectable, large up-down deformation over the width of an actuator caused by stress at the edges of the facesheet when flattening out the large, nominal cylinder term typical of an unpowered MEMS DM. It is unclear why the scalloping appears in the intensity image since it should only be a phase effect at the pupil. Note also the single dead actuator in the lower right of the pupil, which introduces ~2.0 radians of wavefront error to the otherwise flattened entrance pupil phase.

The focal plane image corresponding to the segmented pupil case clearly show the effects of pupil segmentation, as seen in Fig. 12 (left panel). The field stop was temporarily removed for these images (but was then re-inserted to reduce stray light to be able to reach contrasts below 10^{-8}). Nevertheless, it was still possible to use wavefront sensing and control (WFSC) to dig a dark hole (Fig. 12, right). The six diffraction spikes and the majority of the satellite spots seen in Fig. 12 are from the hexagonal pupil segmentation. The bright satellite spots at x = ±44, y = ±44 λ/D are from the periodic surface print-through (also called quilting) of the BMC DM surface (which is present over the entire DM surface.) The whole correction region is a 7.3 λ/D radius semicircle shifted right by 2.9 λ/D to match the opening of the field stop.

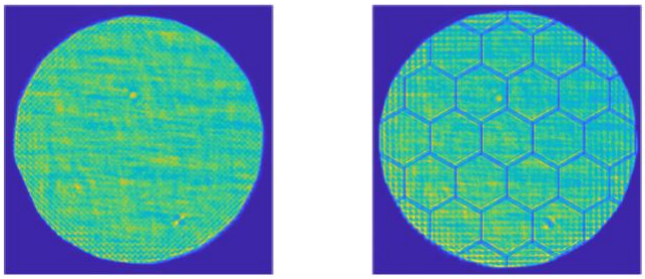

Figure 11. *DST pupil image for (left) the unobscured aperture, and (right) the hexagonally-segmented aperture. The feature in the lower right is from a dead actuator.*

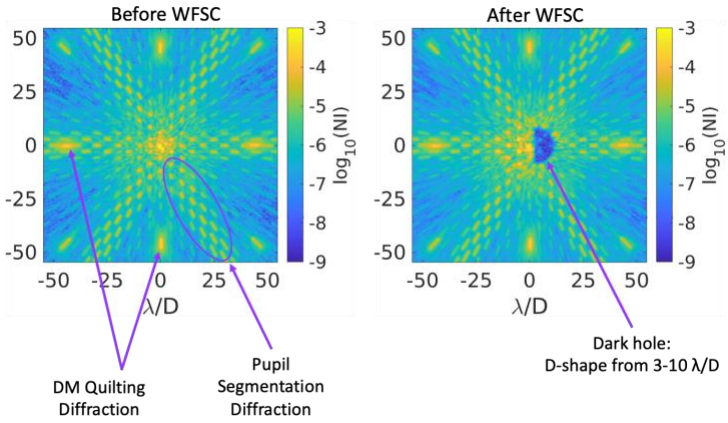

Figure 12. *Extended view of the post-coronagraphic stellar PSF (a) after pupil wavefront flattening but before focal plane WFSC and (b) after focal plane WFSC.*

Using the segmented pupil mask, three milestone runs were carried out, each reaching contrasts below 10^{-8} by about a factor of 2. The evolution of the contrast in these three runs is shown in Fig. 13. The contrast plotted is the ratio of average dark hole level to the starlight level, as described earlier. The positive jumps in contrast seen about every fifth sample in Fig. 13 are due to the regularization scheme that is typically used during an EFC run, known as β-bumping [28], in which the dark hole is made to jump to a worse value to avoid getting stuck in local minima. Note that two of the runs follow each other closely, and so are difficult to resolve, as they are on top of each other, whereas in the third run, an offset in the timing of the beta-bumping allows that run to be more cleanly separated in the plot. The final dark-hole images for each of our three runs are shown in Fig. 14 (remember that the field stop cuts off light beyond the small illuminated field). Note that the use of 2 DMs has even allowed the removal of the effects of segmentation seen in Fig. 12 from these one-sided dark holes. The testbed was extremely stable and repeatable at the level reached, and so the final dark holes of the three different trials seen in Fig. 14 have very similar speckle morphologies.

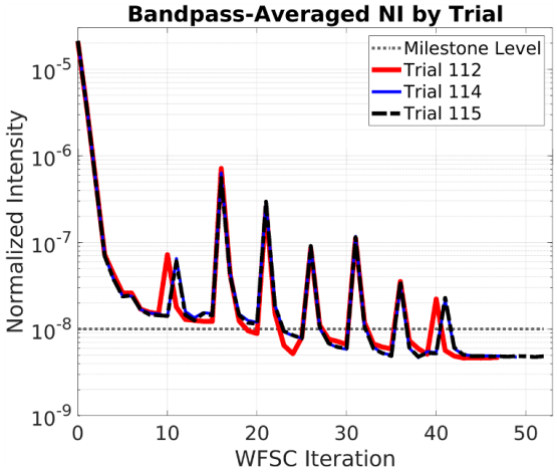

Fig. 13. *Contrast improvement in our dark hole during our three milestone runs. Normalized intensity for the full EFC run; the regularly spaced increases in intensity are due to the β-bumping strategy to reduce the contrast floor.*

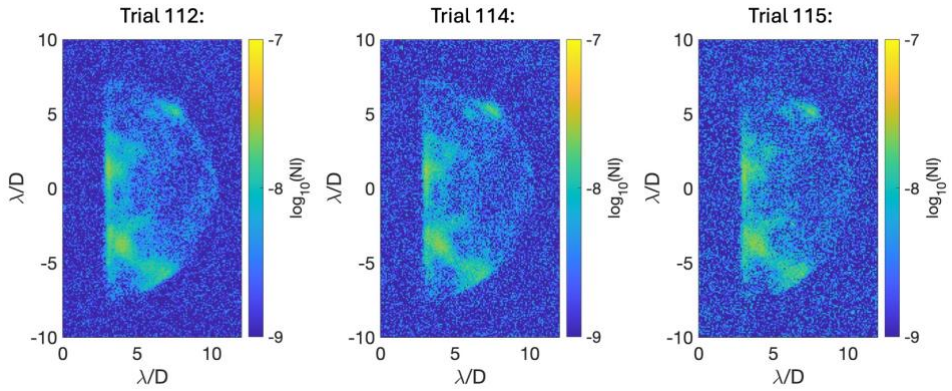

Figure 14. *Intensity images of the final dark-hole regions (set by the size and shape of the field stop) after the last EFC iteration of our three independent runs.*

In our milestone analysis, we used the mean contrasts of the last 5 dark hole frames from each of the three runs. The mean contrasts for each run, their standard deviations, and other significant systematic noise contributors, are given in Table 3. The 90% confidence level is given in the bottom row of the table, where it can be seen that all three contrast results are below the target of 1e-8 by more than the amount needed statistically to meet the milestone criterion. Averaging the three runs together, the final mean contrast obtained is $(4.78 \pm 0.15) \times 10^{-9}$. This is more than 3σ below the milestone target of 1 x 10^{-8}, and is the best contrast result obtained for a vortex coronagraph with a segmented aperture. As with earlier monolithic aperture broadband tests, the limiting factor for these broadband tests seemed to be small off-axis "defects" in the vortex mask which are uncorrectable by the DM in broadband light.

Table 3. *Row 1: Mean dark-hole contrasts averaged over the last 5 iterations of each of our three milestone runs. Row 2: The standard deviation of each measurement series. Row 3: the standard deviation of the mean for each series. Rows 4 and 5: Camera linearity and photometry systematic errors. Row 6: the quadrature sum of rows 3,4 and 5. Row 7 gives the resultant 1.28 sigma levels above the mean for each run, i.e., the 90% confidence level for each run. All three are well below the milestone target of 1 x* 10^{-8}.

	Run 1	Run 2	Run 3
Mean contrast, $\hat{c}$	4.67e-9	4.85e-9	4.82e-9
Sigma_meas	2.83e-11	7.00e-11	4.40e-11
Sigma_mean	1.26e-11	3.13e-11	1.97e-11
Sigma_lin	$0.01\hat{c}$ = 4.67e-11	$0.01\hat{c}$ = 4.85e-11	$0.01\hat{c}$=4.82e-11
Sigma_phot	$0.08\hat{c}$ = 3.74e-10	$0.04\hat{c}$ = 1.94e-10	$0.04\hat{c}$=1.93e-10
Sigma_total	3.76e-10	2.02e-10	2.00e-10
$\hat{c} + 1.28$ Sigma_total	5.15e-9	5.11e-9	5.08e-9

7.2. Milestone 1a Certification Data Package: Monochromatic Starlight Suppression for a clear monolithic input pupil

This section presents our results for a monolithic aperture and a monochromatic laser, using the 2-DM layout of Fig. 9b. A more wide-ranging discussion is provided in ref [29]. In this case, we carried out four milestone runs, for each of which we ran EFC from a flat DM configuration. Fig. 15 shows the final dark hole frame from one of our runs. As can be seen in Fig. 15, the limiting factor in the contrast achievable with narrowband light is a set of concentric rings that resemble a speckled Airy pattern.

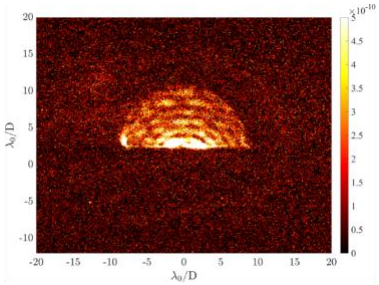

Figure 15. *Intensity image of a final dark-field region (set by the size and shape of the field stop) after the last EFC iteration of one of our runs. The exposure time was 120 s.*

Fig. 16 show the evolution of the mean dark hole contrast for each of our four milestone runs. The contrast plotted is the ratio of dark hole level to the starlight level, as described earlier. The positive jumps in contrast seen every fifth sample in Fig. 16 are again due to β-bumping [28] in which the dark hole is made to jump to a worse value to avoid getting stuck in local minima.

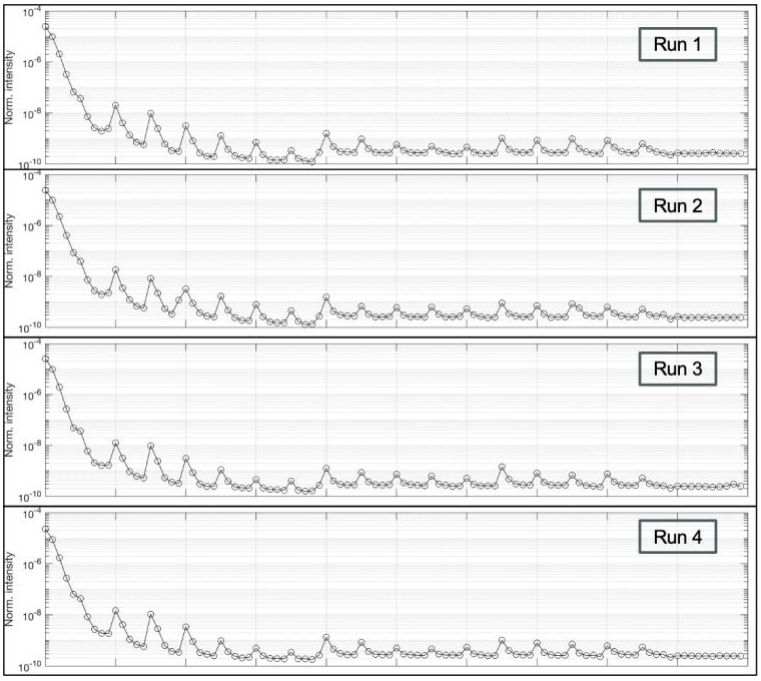

Fig. 16. *Contrast improvement in our dark hole during our four milestone runs. Normalized intensity for the full EFC run; the regularly spaced increases in intensity are due to the β-bumping strategy to reduce the contrast floor*

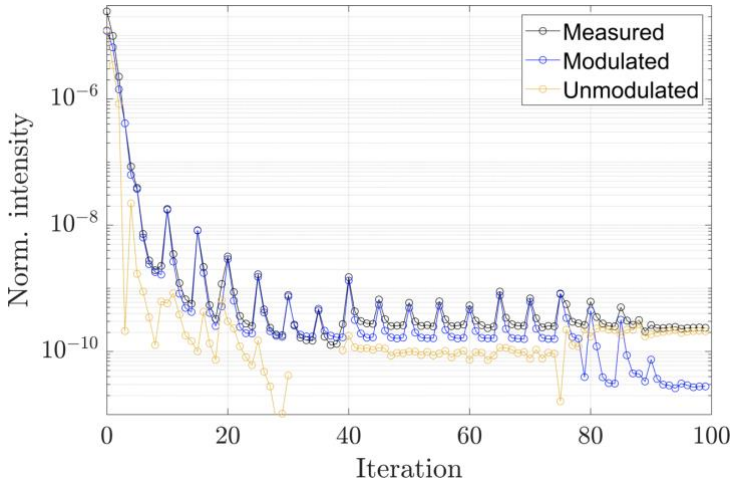

Fig. 17. *Contrast improvement in our dark hole during one of our milestone runs. Normalized intensity for the full EFC run; the regularly spaced increases in intensity are due to the β-bumping strategy to reduce the contrast floor.*

Fig. 17 provides more detail on one of the milestone runs, breaking up the contrast into coherent (modulated by the DM) and incoherent (unaffected by the DM) components. After the integration times were increased to 120 sec near iteration 80, the unmodulated (i.e., steady) component dominates the contrast (this is the component that yields the Airy pattern of Fig. 15). One complete wavefront sensing and control cycle, including overhead for CCD readouts, data handling and computations, thus took about 10 min.

In our milestone analysis, we used the mean contrasts of the last 10 dark hole frames from each of the four runs. The mean contrasts for each run, their standard deviations, and other significant systematic noise contributors, are given in Table 4. The 90% confidence level is given in the bottom row of the table, where it can be seen that all four runs yielded contrast results that are below the target of 3 x 10^{-10} by more than the amount needed statistically to meet the 90% confidence level. Averaging the four runs together, the final mean contrast obtained is $(2.49 \pm 0.14) \times 10^{-10}$. This is more than 3σ below the milestone target of 3 x 10^{-10}, and is the best contrast ever obtained with a vortex coronagraph in monochromatic light. Finally, we note that the contrast level even in the innermost 3-4 λ/D region had an average of ~ 6 x 10^{-10}.

As mentioned, and in contrast to the broadband case discussed earlier, the contrast limit in this monochromatic case is seen to be due to a faint Airy-like ring pattern. Such a pattern in turn implies a light leakage that uniformly fills the pupil plane. Leakage that uniformly fills the pupil could be due either to polarization leakage, i.e., light that was unaffected by the vortex because of the mask's small deviation from a retardance of π radians, or to the lack of a central obscuration on this mask, which would allow a small central point-like region of starlight to diffract and fill the Lyot plane pupil. The next section details future work to be pursued to try to identify the origin of this leakage.

Table 4. *Row 1: Mean dark-hole contrasts averaged over the last 10 iterations of each of our four milestone runs. Row 2: The standard deviation of each measurement series. Row 3: the standard deviation of the mean for each series. Rows 4 and 5: Camera linearity and photometry systematic errors. Row 6: the quadrature sum of rows 3,4 and 5. Row 7 gives the resultant 1.28 sigma levels above the mean for each run, i.e., the 90% confidence level for each run. All four are below the target of 3 x* 10^{-10}.

	Run 1	Run 2	Run 3	Run 4
Mean contrast, $\hat{c}$	2.46e-10	2.45e-10	2.64e-10	2.41e-10
Sigma_meas	0.98e-11	2.24e-11	1.41e-11	1.33e-11
Sigma_mean	3.10e-12	7.08e-12	4.46e-12	4.21e-12
Sigma_lin	2.46e-12	2.45e-12	2.64e-12	2.41e-12
Sigma_phot	1.23e-11	1.23e-11	1.32e-11	1.21e-11
Sigma_total	1.29e-11	1.44e-11	1.42e-11	1.30e-11
$\hat{c} + 1.28$ Sigma_total	2.63e-10	2.63e-10	2.82e-10	2.58e-10

8. Other Masks and their Characterization Tests

Several other masks were fabricated and tested during the course of this work, but the best mask so far, by about a factor of 2, remains the one used in our earlier broadband tests, which is described in Section 3.1.2. As repeatability has been an issue in vortex mask manufacture, some of the masks acquired were aimed specifically at the goal of simpler mask fabrication, as multilayer masks are difficult and time-consuming to fabricate, as seen in Fig. 4. As a result, we have begun to investigate two specific issues (both discussed in more detail in the next paragraphs): the effect of the central blocker, and the effect of allowing the topological charges of the individual vortex layers to differ. The first investigation is aimed at the elimination of an internal layer (which is fabricated by a different vendor) that introduces an undesirable fabrication complication and a jump in layer thickness, and the second issue is aimed at layer tolerance relaxation. Both steps can potentially result in masks that are easier to fabricate. The current status of these efforts is now discussed.

The removal of the central blocker. Common wisdom suggests that because the brightest region of the stellar PSF lands exactly on the vortex mask's central defect, the resultant contrast can likely be improved by covering the central defect with a small opaque blocker [9,20]. On the other hand, our best performance (contrast) results have actually been obtained with a vortex mask without a central blocker, although the performance differences so far have only been on the order of a factor of 2. It would therefore be desirable to establish whether a central blocker is actually needed, as its absence would simplify mask design. However, the tight layer tolerances involved in fabricating a 3-layer mask means that a one-to-one comparison is best done on the same mask. To this end, we designed a mask that can be disassembled. I.e., the black dot is placed on a separate substrate from the vortex layers, and rather than gluing them together, an air gap is left,

with the two substrates held together by a few tacks of glue along the rim (compare Figs. 3 and 18). After carrying out contrast tests in the DST with a fully assembled mask, one can then remove the spots of glue and retest the vortex mask without a central dot. We have carried out some initial tests with the dot in place, but limited testbed time has so far not allowed a complete measurement suite. Once this phase is complete, we will remove the glue tacks, and proceed to the no-dot comparison test.

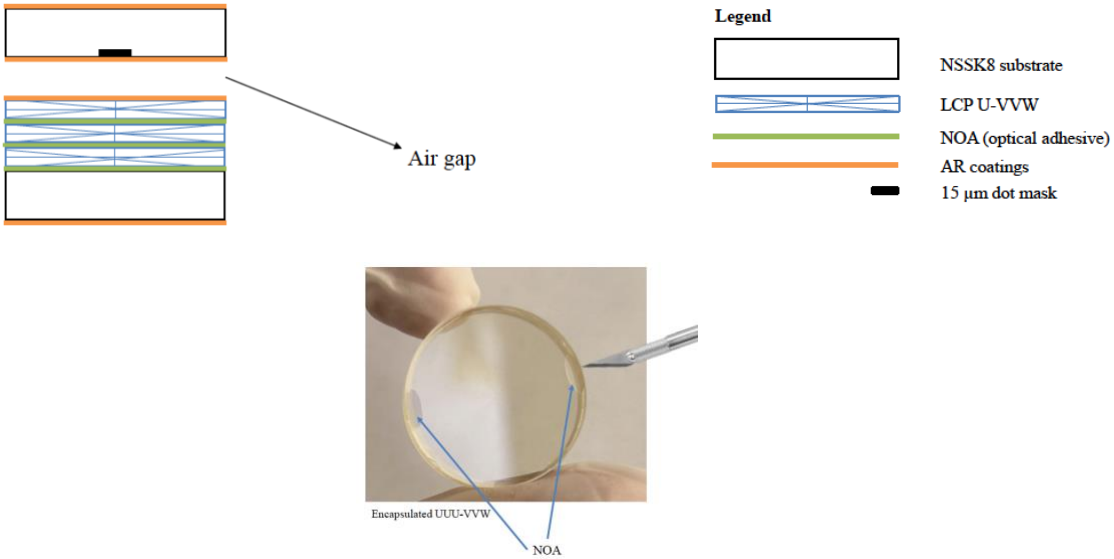

Fig. 18. *Mask cross-section for the case of a removable central opaque spot. An air gap separated two substrates, which are tacked together at their edges. First the mask will be tested assembled as is, and then removing the glue will allow testing of the vortex layers with no central opaque spot in the way.*

Tolerance reduction. A different complication with making standard vortex masks is the extreme accuracy requirements on layer properties such as thickness, which is illustrated in Fig. 19 [30]. These fine layer tolerance requirements make it very difficult to make masks reproducibly to a high degree, and so the approach so far has been to make a large number of masks, so as to get close to the target with at least one of them. However, as this is both time consuming and costly, a different approach would be very beneficial.

In searching parameter space, an interesting discovery was made. Specifically, in the three layer broadband vortex masks fabricated so far, the topological charges of the three layers have always been the same. However, what if they are not? It turns out that dropping this constraint opens up a large new area of parameter space that leads to a very interesting theoretical conclusion. Specifically, some terms in the error budget can be made to disappear if the layers all have differing charges, as three of the seven leakage terms caused by layer inaccuracies change from terms with uniform-phase pupils (which lead to undesirable focal-plane Airy patterns) to vortex-phase terms that send light outside the Lyot-plane pupil stop (Fig. 20), where they can be blocked. If so, the net leakage should be lower with unequal topological charges.

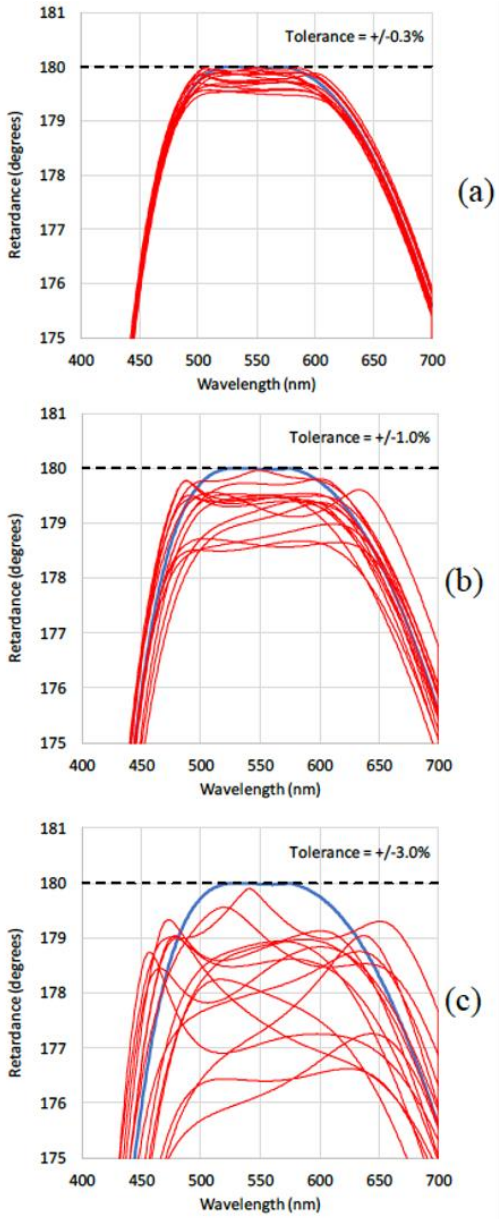

Fig. 19. *Mask retardance vs. wavelength expected for repeated fabrication runs with manufacturing layer tolerances of 0.3% 1.0% and 3.0% (top to bottom).*

As a result, three-layer vortex masks with non-equal charges should leave only a single very dim uniform-pupil leakage term. Moreover, this term, rather than being linearly proportional to any single layer's phase error, is instead proportional to the product of all three small phase errors (one from each layer), and so should itself be much reduced. This in turn should translate to a leakage vs. frequency that can be much broader, with a resultant reduced sensitivity to layer errors, as can be seen in the theoretical predictions of Fig. 21. With relaxed accuracy tolerances, such masks should thus be much easier to manufacture accurately without needing many tries.

$$E_o = \begin{bmatrix} 1 \\ 0 \end{bmatrix}$$

V_1:

$$E_1 = \begin{bmatrix} \eta_1 \\ e^{i2n_1\alpha} \end{bmatrix}$$

V_2:

$$E_2 = \begin{bmatrix} \eta_1\eta_2 + e^{i2(n_1-n_2)\alpha} \\ \eta_1 e^{i2n_2\alpha} + \eta_2 e^{i2n_1\alpha} \end{bmatrix}$$

V_3:

$$E_3 = \begin{bmatrix} \eta_1\eta_2\eta_3 + \eta_3 e^{i2(n_1-n_2)\alpha} + \eta_2 e^{i2(n_1-n_3)\alpha} + \eta_1 e^{i2(n_2-n_3)\alpha} \\ e^{i2(n_1-n_2+n_3)\alpha} + \eta_1\eta_3 e^{i2n_2\alpha} + \eta_2\eta_3 e^{i2n_1\alpha} + \eta_1\eta_2 e^{i2n_3\alpha} \end{bmatrix}$$

= 7 vortex phase terms + 1 small uniform-phase term proportional to the leakage product

If all n's are equal, this becomes

$$E_3 \text{ (equal } n_i) = \begin{bmatrix} \eta_1\eta_2\eta_3 + \eta_3 + \eta_2 + \eta_1 \\ e^{i2(n_1-n_2+n_3)\alpha} + \eta_1\eta_3 e^{i2n_2\alpha} + \eta_2\eta_3 e^{i2n_1\alpha} + \eta_1\eta_2 e^{i2n_3\alpha} \end{bmatrix}$$

~ 4 vortex terms + 3 uniform leakage terms proportional to the first power of leakage

Fig. 20. *The electric field Jones vector in the circular-polarization basis, and its evolution through the three layers of a broadband vortex phase mask (top to bottom). The bottom line gives the simplified field that results if* $n_1 = n_2 = n_3$. *Note that the bottom Jones vector includes 4 terms without phases, but the equation above it for the unequal topological charge case contains only one such term.*

We have manufactured a first mask of this design, and have also carried out initial tests of its contrast performance in the DST. However, the initial contrasts seen with this mask were again within a factor of two of our best "classical" vortex mask. We are investigating why the performance was not at a better level, but the fact that all of the recently fabricated masks of any type yield similar performances (to within about a factor of 2) suggests that it may not actually be the layer thickness and rotation angle errors that are the limiting factor. Delving further into the theory and all error budget terms will be required to understand this result, and this is planned for future work.

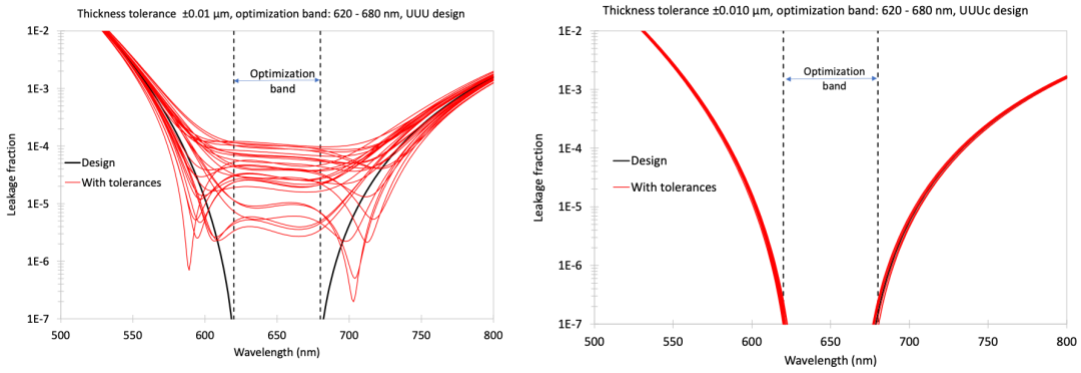

Fig. 21. *Comparison of mask retardances vs. wavelength expected for layer tolerances of 1.0% for "classical" vortex masks with all layer charges equal (left panel) and with three different layer charges (right).*

9. Summary and Prospects

Using a vector vortex phase mask in the DST , we have achieved two milestones: an average monochromatic contrast of $(2.49 \pm 0.14) \times 10^{-10}$ was obtained over a dark-hole extending from 3 – 10 λ/D, for single polarization light at 637 nm wavelength, and with a segmented aperture, a contrast of $(4.78 \pm 0.15) \times 10^{-9}$ was achieved for 10% BW light over the same 3 – 10 λ/D dark hole. Both results are the best of their kind. They are also at significantly better levels than the 90% confidence level.

The limiting leakages in the two cases are different: monochromatic contrast is limited by a faint centered Airy-like pattern that could arise either from polarization leakage or the absence of a central opaque spot, while broadband contrasts are limited by small off-axis features, or defects, that can be reduced with more optimized manufacturing techniques. We plan to continue to investigate these leakage sources in order to push toward still deeper broadband contrasts under TDEM award 23-SAT23-0002.

Acknowledgements

We thank the staff of Beam Engineering for their very significant efforts in devising and fabricating improved LCP-based vortex masks.

This research was carried out at the Jet Propulsion Laboratory, California Institute of Technology, under a contract with the National Aeronautics and Space Administration (80NM0018D0004).

10. References

[1] https://exoplanets.nasa.gov/exep/studies/probe-scale-stdt/

[2] https://www.jpl.nasa.gov/habex/documents/

[3] https://asd.gsfc.nasa.gov/luvoir/reports/

[4] https://www.nationalacademies.org/our-work/decadal-survey-on-astronomy-and-astrophysics-2020-astro2020

[5] https://science.nasa.gov/astrophysics/programs/habitable-worlds-observatory/

[6] https://exoplanets.nasa.gov/internal_resources/1366/

[7] Serabyn, E., Trauger, J., Moody, D., Mawet, D., Liewer, K., Krist, J., Kern, B., "High-contrast imaging results with the vortex coronagraph," *Proc. SPIE* **8864**, 88640Y-1, 2013.

[8] Guyon, O., Pluzhnik, E.A., Kuchner, M.J., Collins, B., and Ridgway, S.T., "Theoretical Limits On Extrasolar Terrestrial Planet Detection with Coronagraphs," *Ap.J. Suppl.* **167,** 81, 2006.

[9] Mawet, D. *et al.*, "Optical Vectorial Vortex Coronagraphs using Liquid Crystal Polymers: Theory, Manufacturing and Laboratory Demonstration," *Optics Express,* **17**, 1902, 2009.

[10] Serabyn E., D. Mawet & R. Burruss, "The potential of small space telescopes for exoplanet observations," *Proc. SPIE* **7731**, 77312O, 2010.

[11] Trauger, J. and W. Traub, "A laboratory demonstration of the capability to image an Earth-like extrasolar planet," *Nature* **446**, 771, 2007.

[12] Levine, M., Shaklan, S. & Kasting, J., "Terrestrial Planet Finder Coronagraph: Science and Technology Definition Team Report," JPL Publ. D-34923, 2006.

[13] Mawet, D., Riaud, P., Absil, O. & Surdej, J., "Annular Groove Phase Mask Coronagraph," *ApJ*, **633**, 1191, 2005.

[14] Swartzlander, G., "The optical vortex coronagraph, " *J. Opt. A.*, **11**, 1464, 2009.

[15] Serabyn, E. & Mawet, D., "Detecting Exoplanets with a Liquid-Crystal-Based Vortex Coronagraph," *Mol. Cryst. Liq. Cryst.* **559**, 69, 2012.

[16] Mawet, D. *et al.*, "Taking the vector vortex coronagraph to the next level for ground- and space-based exoplanet imaging instruments: review of technology developments in the USA, Japan, and Europe," *Proc. SPIE* **8151**, 815108-1, 2011.

[17] Pancharatnam, S., "Achromatic combination of birefringent waveplates," Proc. Indian Acad. Sci. A **41**, 137, 1955.

[18] Tabiryan, N.V., Nersisyan, S.R., Xianyu, H., and Serabyn, E., "Fabricating Vector Vortex Waveplates for Coronagraphy," Proc. 2012 IEEE Aerospace conf., 10.1109/AERO.2012.6187181, 2012

[19] Roberts, D.E., Sigley, J., Ruane, G., Serabyn, E., "Implementing achromatic diffractive waveplate optics with thin, uniformly birefringent layers" Proc. 2022 IEEE Aerospace conf., 10.1109/AERO53065.2022.9843574, 2022

[20] Serabyn, E. *et al.,* "Vector vortex coronagraphy for exoplanet detection with spatially variant diffractive waveplates," JOSA B **36**, D13, 2019.

[21] Ruane, G. *et al*. (2022), "Broadband Vector Vortex Coronagraph Testing at NASA's High Contrast Imaging Testbed Facility, Proc. SPIE **12180**, 1218024

[22] Ruane, G. *et al.,* "Decadal Survey Testbed Commissioning Roadmap: Demonstrating Technology for Imaging New Worlds," https://exoplanets.nasa.gov/internal_resources/1170/, 2019.

[23] Patterson, K. D., et al., "Design description and commissioning performance of a stable coronagraph technology development testbed for direct imaging of Earth-like exoplanets," in Proc. SPIE **11117**, 111171U, 2019.

[24] Give'on, A., Kern, B., Shaklan, S., Moody, D. C., and Pueyo, L., "Broadband wavefront correction algorithm for high-contrast imaging systems," in Proc. SPIE **6691**, 63 – 73, 2007.

[25] Riggs, A. J. E., Ruane, G., Sidick, E., Coker, C., Kern, B. D., and Shaklan, S. B., "Fast linearized coronagraph optimizer (FALCO) I: a software toolbox for rapid coronagraphic design and wavefront correction," in Proc. SPIE **10698**, 106982V, 2018.

[26] Trauger, J. *et al*., "ACCESS – A Concept Study for the Direct Imaging and Spectroscopy of Exoplanetary Systems," in "Pathways towards Habitable Planets," *ASP Conf. Ser.* **430***,* 375, 2010.

[27] Riggs, A.J. et al. "High-contrast demonstration of a vector vortex coronagraph with a segmented, off-axis aperture", in Proc. SPIE vol. **12180**, 121805I, 2022.

[28] Seo, B.-J., "Testbed demonstration of high-contrast coronagraph imaging in search for Earth-like exoplanets," in Proc. SPIE **11117**, 599 – 609, 2019.

[29] Llop-Sayson, J., Ruane, G., Serabyn, E., Mejia Prada, C., Walter, A., Allan, G. "Vector Vortex Coronagraph Experiments in Vacuum Towards 10^{-10} Contrast," in Proc. SPIE **13092**, 130921Y, 2024.

[30] Roberts, D. Xianyu, H., Nersisyan, S., Tabiryan, N.V., Xianyu, H., Serabyn, E., "Overcoming the tradeoff between efficiency and bandwidth for vector vortex waveplates," Proc. 2019 IEEE Aerospace conf., 10.1109/AERO.2019.8741585, 2019.